applied sciences

MDPI

Article

Active Tunable Elastic Metasurface for Abnormal Flexural Wave Transmission

Bizun Lin [1], Jingru Li [1,*], Wei Lin [2,3] and Qingfen Ma [1]

[1] School of Mechanical and Electrical Engineering College, Hainan University, Haikou 570228, China
[2] College of Shipbuilding Engineering, Harbin Engineering University, Harbin 150006, China
[3] Qingdao Innovation and Development Center, Harbin Engineering University, Qingdao 266000, China
* Correspondence: ljr@hainanu.edu.cn

Abstract: An active elastic metasurface has more flexibility than a passively modulated elastic metasurface, owing to the manipulation of the phase gradient that can be realized without changing the geometrical configuration. In this study, a negative proportional feedback control system was employed to provide positive active control stiffness for adaptive unit cells, with the aim of achieving the active modulation of the phase gradient. The relationship between the control gain and the phase velocity of the flexural wave was derived, and the transfer coefficients and phase shifts of the flexural wave through the adaptive unit cells were resolved using the transfer matrix method. Finite element simulations for wave propagations in the adaptive unit cells were conducted, and they verified the analytic solutions. Based on this theoretical and numerical work, we designed active elastic metasurfaces with adaptive unit cells with sub-wavelength thicknesses according to the generalized Snell's law. These metasurfaces show flexibility in achieving abnormal functions for transmitted waves, including negative refraction and wave focusing, and transforming guided waves at different operating frequencies by manipulating the control gain. Therefore, the proposed active metasurface has great potential in the fields of the tunable manipulation of elastic waves and the design of smart devices.

Keywords: active elastic metasurface; flexural wave controlling; feedback control gain; generalized Snell's law; piezoelectric effects

Citation: Lin, B.; Li, J.; Lin, W.; Ma, Q. Active Tunable Elastic Metasurface for Abnormal Flexural Wave Transmission. *Appl. Sci.* **2024**, *14*, 2717. https://doi.org/10.3390/app14072717

Academic Editor: Muamer Kadic

Received: 11 January 2024
Revised: 10 March 2024
Accepted: 18 March 2024
Published: 24 March 2024

1. Introduction

Metasurfaces [1–5] are artificially constructed materials with subwavelength thicknesses in the direction of wave propagation, exhibiting an excellent ability to manipulate wavefronts, as well as having a more compact physical space and simplicity compared to conventional metamaterials [6–10]. Metasurfaces have been widely used in various fields, such as medical imaging, holographic imaging, and signal processing, following studies on their extraordinary beam modulation ability in the fields of electromagnetics [11–13] and acoustics [14–19]. Recently, the research on metasurfaces has been expanded to the field of elastic waves [20–28]. However, elastic waves possess more degrees of freedom during solid propagation [29–31], which leads to a great challenge for researchers. Determining a method to extract and control the propagation of specific modes of guided waves from multimodal guided waves in a solid has become a hot research topic.

Researchers have designed elastic wave metasurfaces based on the generalized Snell's law (GSL) for wavefront modulation behaviors such as abnormal refraction, wave focusing, and Bessel waves. Zhu et al. [21] first proposed metasurfaces for the abnormal deflection of A_0 Lamb waves. Lee et al. [26] utilized the relationship between the effective mass and stiffness to achieve the modulation of transmitted traveling waves. Classical zigzag topology was used to alter the propagation path of flexural waves, taking advantage of the different propagation paths of the flexural wave to realize the phase shift of the basic unit

cell across the full 2π [23]. A series of abnormal modulation behaviors of the flexural wave was realized by adjusting the phase gradient. A structure for the passive modulation of multi-mode guided waves was achieved by adding different lengths of cover layers on the unit element, and the theoretical analysis was verified by finite element simulations and experiments [25].

The above case can be identified as the passive modulation [32–36] of elastic waves. Passive modulation requires a change in the phase gradient by changing the geometry after fixing the phase distribution, which makes metasurfaces much less practical. Therefore, adaptive elastic metasurfaces have attracted considerable interest. Si-Min Yuan et al. [37] proposed a nuts-and-screws structure where the tunability of the phase shift is induced by the screw-in depth based on the dispersion theory of locally resonant phononic crystals. By adjusting the position of the nut on the screw to achieve the full 2π coverage of the phase shift of the functional element, the abnormal refraction and wave-focusing functions of the broadband plate wave were achieved based on the GSL without re-fabricating the metasurface. There are various ways to use piezoelectric materials for active modulation. Piezoelectric patches can be stacked together to form a unit cell, which can be adjusted via negative capacitance circuits connected to achieve a wide frequency range of elastic longitudinal waves with a variety of modulation functions. It is also possible to attach a piezoelectric sheet to the substrate material and use electromechanical tuning to modulate the propagation of asymmetric mode Lamb waves [38]. Shixuan Shao et al. [39] presented a novel metasurface that is proposed to simultaneously manipulate multi-mode guided waves in the plate, including shear horizontal waves, symmetric mode, and anti-symmetric mode Lamb waves. Monolithic in-plane and out-of-plane polarized piezoelectric metasurface sheets were staggered on both faces of the substrate, and each piezoelectric patch was individually connected to a negative capacitance circuit. The metasurface can be multifunctionally modulated in each mode by adjusting the shunt's negative capacitance.

Currently, most metasurfaces are actively modulated by negative-capacitance circuits, but negative-capacitance circuits are difficult to achieve in real-word applications. In order to satisfy the requirement of modulating wave transmission in real time, the piezoelectric patches were attached at the upper and lower surfaces of the unit cells, with the upper surface's piezoelectric patch acting as a brake, the lower surface piezoelectric patch acting as a sensor, and the piezoelectric patch externally connected to a negative proportional feedback control strategy [40]. This strategy was employed to provide positive active control stiffness to the piezoelectric sensor/actuator patch in the present work. This method can be utilized to implement anomalous wave manipulations in an active manner [37,41,42] for the flexural wave. In such systems, the key is to exploit the relationship between flexural wave phase velocity and stiffness by controlling the equivalent stiffness to determine the phase velocity. We derived the relationship between the equivalent stiffness and the phase velocity of the flexural wave and analyzed the transmission coefficients and phase shifts of each cell using the transfer matrix method. Based on the GSL, the adaptive unit cells were cleverly arranged to construct appropriate phase gradients, thus enabling the abnormal refraction [43,44], focusing [45–48], and transforming the guided wave of the metasurface to be realized at different frequencies.

The paper is organized as follows. Section 2 outlines the theoretical derivation of the adaptive unit cell and metasurface design. Section 3 demonstrates the abnormal modulation of flexural waves via metasurfaces through finite element simulations. Section 4 summarizes some conclusions.

2. Mechanisms of Actively Tunable Elastic Metasurface

2.1. Description of Adaptive Unit Cells

We used a negative proportional feedback control strategy to modulate the phase of the adaptive unit cells, which can control the flexural wave more efficiently and contribute to the fabrication of the metasurface. The proposed adaptive unit cell is shown in Figure 1, where Figure 1a shows the three-dimensional geometric model of the adaptive unit cell

and Figure 1b shows the two-dimensional model. From Figure 1a, it can be seen that the adaptive unit cell contains two sub-cells. The gray and yellow regions indicate the base beam (aluminum) and the piezoelectric patch, respectively; the upper part of the piezoelectric patch is used as the piezoelectric sensor, and the lower part is applied as the piezoelectric actuator. Moreover, the negative proportional feedback control system is connected externally to the piezoelectric patch. The ratio of the sensed voltage generated by the deformation of the sensor to the external voltage applied by the control system is used to realize the positive active stiffness gain [40]. In the adaptive unit cell of length $L = l_1 + l_2$, the lengths of sub-cell 1 (l_1) and sub-cell 2 (l_2) are adjustable, and we define l_1/L as p. The thickness of the base beam in sub-cell 1 is h_{s1} and that in sub-cell 2 is h_{s2}, and the two substrates are covered with piezoelectric patches with a thickness of h_p. The width of the piezoelectric patch is the same as the width of the base beam. The total thickness of sub-cell 1 is $h_1 = h_{s1} + 2h_p$ and the total thickness of sub-cell 2 is $h_2 = h_{s2} + 2h_p$.

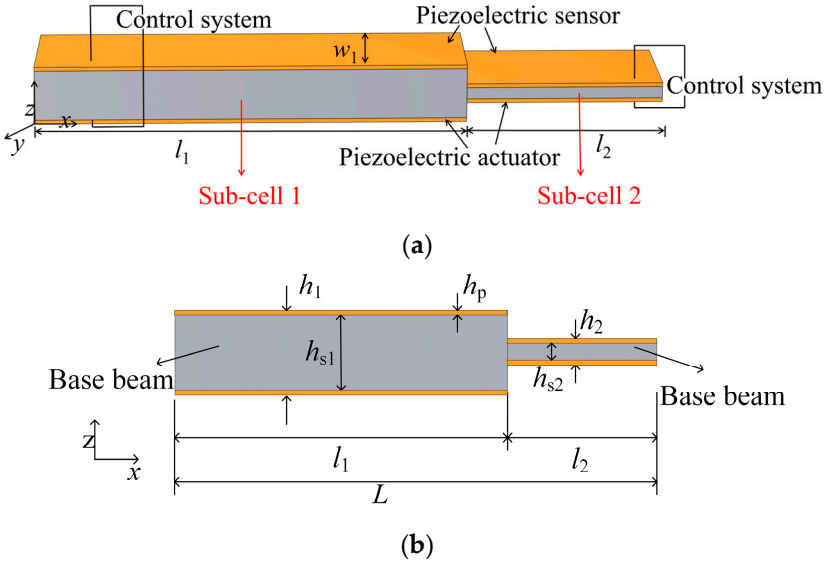

Figure 1. (**a**) A 3D model of the adaptive unit cell with a negative proportional feedback control strategy. (**b**) A 2D model of the 3D adaptive unit cell in (**a**).

2.2. Derivations of the Governing Equation

The constitutive equation of piezoelectric materials can be expressed as follows:

$$\begin{aligned} S_i &= s_{ij}T_j - d_{in}E_n \\ D_m &= d_{mj}T_j + \varepsilon_{mn}E_n \end{aligned} \quad (i, j = 1, 2, 3, 4, 5, 6; m, n = 1, 2, 3) \tag{1}$$

where $\boldsymbol{S}$ is mechanical strain, $\boldsymbol{T}$ is mechanical stress, $\boldsymbol{D}$ is electrical displacement, $\boldsymbol{E}$ is the electric field, s_{ij} is the flexibility coefficient under constant electric field conditions, d is the piezoelectric stress constant, and ε_{mn} is the dielectric constant. The correspondence between the numerical subscripts and the coordinate axes is 1→x, 2→y, 3→z, 4→yz, 5→xz, 6→xy.

In the piezoelectric sheet used in this study, the polarization surface is perpendicular to the z-axis, and the action of the electric field in the z-axis direction is mainly considered, ignoring the electric field in the x-axis and y-axis directions, which implies that $E_1 = E_2 = 0$. The piezoelectric sheet is constrained in the x-y plane, with the stress relation $T_3 = T_4 = T_5 = 0$. The piezoelectric material is transverse isotropic in the x-y plane, and it can be shown that $s_{11} = s_{22}$.

Consider a piezoelectric material; its constitutive equations can be expressed as [42]

$$\begin{aligned} S_1 &= s_{11}T_1 - d_{31}E_3 \\ D_3 &= d_{31}T_1 + \varepsilon_{33}E_3 \end{aligned} \tag{2}$$

It is worth noting that the potential D_3 is constant at the electrode with area A_s [49,50]. According to the classical laminated beam theory, the equivalent density ρ_a and the equivalent stiffness D_a of the laminated composite beam with the piezoelectric material can be written as [40]

$$\rho_a = \rho_s h_s + 2\rho_p h_p \tag{3}$$

$$D_a = \frac{E_s h_s^3}{12(1-v_s^2)} + 2c_{11}(A_s I_1^2 + \frac{w_1 h_p^3}{12}) \tag{4}$$

where ρ_s, E_s, and v_s are the mass density, Young's modulus, and Poisson's ratio of the substrate material, respectively; ρ_p is the density of the piezoelectric material; w_1 is the width of the adaptive unit cell; h_s is the thickness of the base beam; and $I_1 = (h_p + h_s)/2$.

Following Euler's beam theory, the vibration equation of a composite beam with a piezoelectric actuator and sensors is

$$D_a \frac{\partial^4 w(x,t)}{\partial x^4} + \rho_a h \frac{\partial^2 w(x,t)}{\partial t^2} + \frac{d_{31} I_1}{h_p} \frac{\partial^2 Y_a}{\partial x^2} - \frac{d_{31} I_1}{h_p} \frac{\partial^2 Y_s}{\partial x^2} = 0 \tag{5}$$

where Y_a is the external voltage applied by the control system and Y_s is the sensed voltage generated by the deformation of the sensor.

The sensed voltage of the piezoelectric sensor Y_s produced by the deformation of the composite base beam can be given by [50]

$$Y_s = -\frac{d_{31} I_1}{\varepsilon_{33} w_1} \frac{\partial^2 w}{\partial x^2} \tag{6}$$

where ε_{33} is the dielectric constant of the piezoelectric material and d_{31} is the piezoelectric stress constant of the piezoelectric material. The metasurface adaptive unit cells were designed using a negative proportional feedback control strategy. The sensing voltage Y_s caused by the deformation of the piezoelectric sensor is measured and fed back to the piezoelectric actuator as an external control voltage. Therefore, the relationship between the external control voltage Y_a and the sensing voltage Y_s can be expressed as

$$Y_a = -gY_s = g\frac{d_{31} I_1}{\varepsilon_{33} w_1} \frac{\partial^2 w}{\partial x^2} \tag{7}$$

where g is the proportional feedback control gain of the piezoelectric actuator. The active stiffness can be generated by an external control voltage applied to the piezoelectric actuator, which can manipulate the flexural wave propagation characteristics of the adaptive unit cell. The variation in g is also limited to 0~100 in order to maintain the stability of the constant voltage electric field.

Substituting Equations (6) and (7) into Equation (5), the coupled equation can be obtained as

$$D_{a1} \frac{\partial^4 w(x,t)}{\partial x^4} + \rho_a h \frac{\partial^2 w(x,t)}{\partial t^2} = 0 \tag{8}$$

where D_{a1} is the equivalent stiffness of the beam with the piezoelectric actuator and sensor acting together and can be written as

$$D_{a1} = D_a + (1+g)\frac{d_{31}^2 I_1^2}{\varepsilon_{33} w_1 h_p} \tag{9}$$

The separable solution to Equation (8) can be written as $w(x,t) = w(x)e^{i\omega t}$, where ω is $2\pi f$. Substituting this solution and Equation (9) into Equation (8), the control equation for the flexural wave can be obtained as

$$\frac{\partial^4 w(x)}{\partial x^4} - k^4 \frac{\partial^2 w(x)}{\partial t^2} = 0 \tag{10}$$

where k is the wavenumber and k^4 is expressed as

$$k^4 = \frac{\rho_a h \omega^2}{D_{a1}} \tag{11}$$

The phase velocity c for the flexural wave is

$$c = \left(\frac{D_{a1} \omega^2}{\rho_a h} \right) \tag{12}$$

Equation (12) indicates that flexural waves are dispersive, and their phase velocity depends on the flexural stiffness. In designing the metasurface, we can vary the magnitude of the gain using a negative proportional feedback control system to obtain the desired phase velocity.

2.3. Generalized Snell's Law

According to the generalized Snell's law, the relationship between the incident and transmitted angles of a flexural wave passing through the metasurface is as follows

$$\frac{\sin(\theta_t)}{\lambda_t} - \frac{\sin(\theta_i)}{\lambda_i} = \frac{1}{2\pi} \frac{\mathrm{d}\varphi_y}{\mathrm{d}y} \tag{13}$$

where $\lambda_i = c/f$, θ_i and θ_t are the incident and transmitted angles, respectively; λ_i and λ_t are the wavelength of the incident and transmitted flexural waves, respectively; and $d\varphi_y/\mathrm{d}y$ is the phase gradient along the y-axis.

The wavelengths of the incident and transmitted regions are the same when the same material is applied, and hence $\lambda_i = \lambda_t$. Equation (13) can be organized as

$$\frac{\sin(\theta_t) - \sin(\theta_i)}{\lambda_i} = \frac{1}{2\pi} \frac{\mathrm{d}\varphi_y}{\mathrm{d}y} \tag{14}$$

In particular, if the wave is incident vertically, the magnitude of the angle of refraction is calculated according to the following formula:

$$\theta_t = \arcsin\left(\frac{\lambda_t}{2\pi} \times \frac{d\varphi_y}{dy} \right) \tag{15}$$

2.4. Focusing Principle

For a certain focal position (x_0, y_0), the phase distribution along the metasurface is

$$\varphi_y = k_i(\sqrt{(y - y_0)^2 + {x_0}^2} - x_0) + \varphi_{y_0} \tag{16}$$

where y_0 is the transverse coordinate of the focal point O, x_0 is the distance from the focal point O, φ_y is the phase, and k_i is the wavenumber in the incident region plate. When designing the focal point $y_0 = 0$, the focusing equation can be simplified as

$$\varphi_y = k_i(\sqrt{y^2 + {x_0}^2} - x_0) \tag{17}$$

2.5. Theoretical Formulations of the Transmission Matrix Method

In this subsection, we will use the transmission matrix method (TMM) to resolve the transmission coefficients and phase shifts of the unit cell. It has been shown that the transmission coefficient and phase shift of a three-dimensional model is equivalent to those of a two-dimensional model [44]. Therefore, the wave propagation can be considered as a

plane strain problem in the xz plane, which is independent of the y-axis direction, as shown by the basic unit in Figure 2. The general solution to Equation (10) is

$$w(x) = a_+e^{-ikx} + a_-e^{ikx} + b_+e^{-kx} + b_-e^{kx} \tag{18}$$

where a_+e^{-ikx} and b_+e^{-kx} are positive propagating and attenuating waves, respectively, and a_e^{ikx} and b_e^{kx} are negative propagating and attenuating waves, respectively. a_+, $a\_$, b_+, and $b\_$ represent the complex coefficients. The displacement $w(x)$, slope $\theta(x)$, bending moment $M(x)$, and shear force $V(x)$ compose the state vector $\mathbf{V} = \{w, \theta, M, V\}^{\mathrm{T}}$.

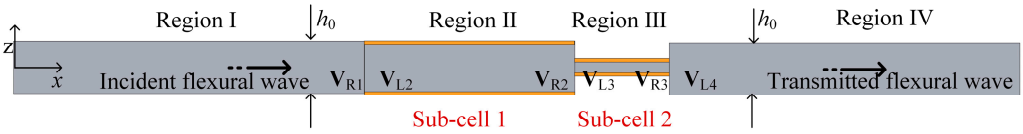

Figure 2. The basic unit for deriving the transmission coefficient and the phase shift.

The basic unit in Figure 2 can be divided into four regions, where region I is the incident region; regions II and III are sub-cell 1 and sub-cell 2, respectively; and region IV is the transmission region. Each region shares the same central axis. The materials of region I and IV are the same as the base beam material with thickness $h_0 = h_1$. As shown in Figure 2, the state vectors on the left and right sides of the connection between the regions working together can be defined as $\mathbf{V}_{R1}$, $\mathbf{V}_{L2}$, $\mathbf{V}_{R2}$, $\mathbf{V}_{L3}$, and $\mathbf{V}_{R3}$ and $\mathbf{V}_{L4}$. The connectivity at the boundaries can be determined from the fact that $\mathbf{V}_{R1} = \mathbf{V}_{L2}$, $\mathbf{V}_{R2} = \mathbf{V}_{L3}$ and $\mathbf{V}_{R3} = \mathbf{V}_{L4}$.

In this way, $\mathbf{V}_{L2}$ can be expressed as

$$\mathbf{V}_{L2} = \begin{bmatrix} 1 & 1 & 1 & 1 \\ -ik_2 & ik_2 & -ik_2 & k_2 \\ -D_2k_2^2 & -D_2k_2^2 & D_2k_2^2 & D_2k_2^2 \\ D_2k_2^3 & -iD_2k_2^3 & -D_2k_2^3 & D_2k_2^3 \end{bmatrix} \begin{bmatrix} a_{+2} \\ a_{-2} \\ b_{+2} \\ b_{-2} \end{bmatrix} \tag{19}$$

where k_2 is the wavenumber in region II and D_2 is the flexural rigidity of region II. According to the above equation, $\mathbf{V}_{L2}$ can be expressed as $\mathbf{V}_{L2} = \mathbf{N}_2\mathbf{A}$, which can be obtained as $\mathbf{A} = \mathbf{N}_2^{-1}\mathbf{V}_{L2}$.

Similarly, $\mathbf{V}_{R2}$ can be written as

$$\mathbf{V}_{R2} = \begin{bmatrix} e^{-ik_2l_1} & e^{ik_2l_1} & e^{-k_2l_1} & e^{k_2l_1} \\ -ik_2e^{-ik_2l_1} & ik_2e^{ik_2l_1} & -k_2e^{-k_2l_1} & k_2e^{k_2l_1} \\ -D_2k_2^2e^{-ik_2l_1} & -D_2k_2^2e^{ik_2l_1} & D_2k_2^2e^{-k_2l_1} & D_2k_2^2e^{k_2l_1} \\ iD_2k_2^3e^{-ik_2l_1} & -iD_2k_2^3e^{ik_2l_1} & -D_2k_2^3e^{-k_2l_1} & D_2k_2^3e^{k_2l_1} \end{bmatrix} \begin{bmatrix} a_{+2} \\ a_{-2} \\ b_{+2} \\ b_{-2} \end{bmatrix} \tag{20}$$

For brevity, $\mathbf{V}_{R2}$ can be expressed as $\mathbf{V}_{R2} = \mathbf{M}_2\mathbf{A}$. Combining Equations (19) and (20) leads to $\mathbf{V}_{R2} = \mathbf{M}_2\,\mathbf{N}_2^{-1}\mathbf{V}_{L2} = \mathbf{U}_2\,\mathbf{V}_{L2}$.

With respect to $\mathbf{V}_{R3}$, there is the following mathematical relationship.

$$\mathbf{V}_{L3} = \begin{bmatrix} e^{-ik_3l_1} & e^{ik_3l_1} & e^{-k_3l_1} & e^{k_3l_1} \\ -ik_3e^{-ik_3l_1} & ik_3e^{ik_3l_1} & -k_3e^{-k_3l_1} & k_3e^{k_3l_1} \\ -D_3k_3^2e^{-ik_3l_1} & -D_3k_3^2e^{ik_3l_1} & D_3k_3^2e^{-k_3l_1} & D_3k_3^2e^{k_3l_1} \\ iD_3k_3^3e^{-ik_3l_1} & -iD_3k_3^3e^{ik_3l_1} & -D_3k_3^3e^{-k_3l_1} & D_3k_3^3e^{k_3l_1} \end{bmatrix} \begin{bmatrix} a_{+3} \\ a_{-3} \\ b_{+3} \\ b_{-3} \end{bmatrix} \tag{21}$$

where k_3 is the wavenumber in region III and D_3 is the flexural rigidity of region III. According to the above equation, $\mathbf{V}_{L3}$ can be expressed as $\mathbf{V}_{L2} = \mathbf{N}_3\mathbf{A}$, which can be obtained as $\mathbf{A} = \mathbf{N}_3^{-1}\mathbf{V}_{L3}$.

The state vector $\mathbf{V}_{R3}$ can be expressed by the following equation:

$$\mathbf{V}_{R3} = \begin{bmatrix} e^{-ik_3(l_1+l_2)} & e^{ik_3(l_1+l_2)} & e^{-k_3(l_1+l_2)} & e^{k_3(l_1+l_2)} \\ -ik_3e^{-ik_3(l_1+l_2)} & ik_3e^{ik_3(l_1+l_2)} & -k_3e^{-k_3(l_1+l_2)} & k_3e^{k_3(l_1+l_2)} \\ -D_3k_3^2e^{-ik_3(l_1+l_2)} & -D_3k_3^2e^{ik_3(l_1+l_2)} & D_3k_3^2e^{-k_3(l_1+l_2)} & D_3k_3^2e^{k_3(l_1+l_2)} \\ iD_3k_3^3e^{-ik_3(l_1+l_2)} & -iD_3k_3^3e^{ik_3(l_1+l_2)} & -D_3k_3^3e^{-k_3(l_1+l_2)} & D_3k_3^3e^{k_3(l_1+l_2)} \end{bmatrix} \begin{bmatrix} a_{+3} \\ a_{-3} \\ b_{+3} \\ b_{-3} \end{bmatrix} \quad (22)$$

According to the above equation, $\mathbf{V}_{R3}$ can be expressed as $\mathbf{V}_{R3} = \mathbf{M}_3\mathbf{A}$, and from Equations (21) and (22), it can be expressed as $\mathbf{V}_{R3} = \mathbf{M}_3\,\mathbf{N}_3^{-1}\mathbf{V}_{L2} = \mathbf{U}_3\,\mathbf{V}_{L2}$.

The above equation gives the following relationship

$$\mathbf{V}_{L4} = \mathbf{V}_{R4} = \mathbf{U}_3\mathbf{V}_{L3} = \mathbf{U}_3\mathbf{V}_{R2} = \mathbf{U}_3\mathbf{U}_2\mathbf{V}_{L2} = \mathbf{U}_3\mathbf{U}_2\mathbf{V}_{R1} \quad (23)$$

It is possible to solve for the transmission coefficients and phase shifts of the flexural waves from Equation (23). For this purpose, the wavefields in regions I, II, III and IV are prepared as follows:

$$\begin{aligned} w_1(x) &= e^{-ik_1x} + re^{ik_1x} + r^*e^{ik_1x} \\ w_2(x) &= a_{+2}e^{-ik_2x} + a_{-2}e^{ik_2x} + b_{+2}e^{-k_2x} + b_{-2}e^{k_2x} \\ w_3(x) &= a_{+3}e^{-ik_3x} + a_{-3}e^{ik_3x} + b_{+3}e^{-k_3x} + b_{-3}e^{k_3x} \\ w_4(x) &= te^{-ik_4x} + t^*e^{-k_4x} \end{aligned} \quad (24)$$

where r, r^*, t, and t^* are the amplitude ratios of the reflected propagating wave, the reflected attenuating wave, the transmitted propagating wave, and the transmitted attenuating wave to the incident wave, respectively. k_4 is the wavenumber in region IV, and k_1 is the wavenumber in region I.

The equation of the $\mathbf{V}_{R1}$ relationship is as follows:

$$\mathbf{V}_{R1} = \begin{bmatrix} 1 & 1 \\ ik_1 & k_1 \\ -D_1k_1^2 & D_1k_1^2 \\ -iD_1k_1^3 & D_1k_1^3 \end{bmatrix} \begin{bmatrix} r \\ r^* \end{bmatrix} + \begin{bmatrix} 1 \\ -ik_1 \\ -D_1k_1^2 \\ iD_1k_1^3 \end{bmatrix} \quad (25)$$

where D_1 is the flexural rigidity of region I. According to the above equation, the mathematical relationship of $\mathbf{V}_{R1}$ can be written as $\mathbf{V}_{R1} = \mathbf{U}_1\mathbf{r} + \mathbf{H}_1$.

$\mathbf{V}_{L4}$ can be expressed as

$$\mathbf{V}_{L4} = \begin{bmatrix} e^{-ik_4(l_1+l_2)} & e^{-k_4(l_1+l_2)} \\ -ik_4e^{-ik_4(l_1+l_2)} & -k_4e^{-k_4(l_1+l_2)} \\ -D_4k_4^2e^{-ik_4(l_1+l_2)} & D_4k_4^2e^{-k_4(l_1+l_2)} \\ iD_4k_4^3e^{-ik_4(l_1+l_2)} & -D_4k_4^3e^{-k_4(l_1+l_2)} \end{bmatrix} \begin{bmatrix} t \\ t^* \end{bmatrix} \quad (26)$$

where D_4 is the flexural rigidity of region IV. According to the above equation, $\mathbf{V}_{L4}$ can be expressed as $\mathbf{V}_{L4} = \mathbf{U}_4\mathbf{t}$.

Combining Equations (23) and (25) leads to

$$\mathbf{U}_3\mathbf{U}_2\mathbf{U}_1\mathbf{r} + \mathbf{U}_3\mathbf{U}_2\mathbf{H}_1 = \mathbf{U}_4\mathbf{t} \quad (27)$$

According to the above equation, the following relationship can be obtained:

$$[\mathbf{U}_4 - \mathbf{U}_3\mathbf{U}_2\mathbf{U}_1]\begin{bmatrix} \mathbf{t} \\ \mathbf{r} \end{bmatrix} = \mathbf{U}_3\mathbf{U}_2\mathbf{H}_1 \quad (28)$$

Based on this equation, the solutions for r, r^*, t, and t^* can be solved computationally. Since the same bending stiffness is present in regions I and IV, $|t|^2$ is taken to calculate the transmission coefficient. The phase can be calculated with the following equation [8].

$$\varphi = \begin{cases} \arctan(\frac{\mathrm{Im(t)}}{\mathrm{Re(t)}}) + \frac{\pi}{2} \\ \arctan(\frac{\mathrm{Im(t)}}{\mathrm{Re(t)}}) + \frac{3\pi}{2} \ \mathrm{Re}(t) < 0 \end{cases} \quad (29)$$

where "Im" and "Re" are the functions to extract the imaginary and real parts, respectively.

3. Numerical Results and Discussion

3.1. The Validation of Transmittance and Phase Shift

The effects of control gain (g) and p-values on the phase shift and transmission coefficient were investigated separately for an operating frequency of 6 kHz. The two-dimensional basic cell shown in Figure 2 was constructed in COMSOL (plane strain module) to calculate the transmission coefficient and phase shift of the adaptive unit cell, and the structural parameters are shown in Table 1. The substrate of the adaptive unit cell is made of aluminum materials whose surfaces are covered with piezoelectric materials. The density, elastic modulus, and Poisson's ratio of aluminum materials are ρ_s = 2700 kg/m^3, E_p = 70 GPa, and υ = 0.33. A piezoelectric material with mass density ρ_p = 7700 kg/m^3, elasticity constant c_{11} = 70.6 Gpa, piezoelectric constant $d_{31} = -12.6374$ C/m^2, and dielectric constant $\varepsilon_{33} = 1.59 \times 10^{-8}$ F/m was adopted in the present work [50]. A unit stress is applied in the $-$z direction to the leftmost interface of region I. The grid size is one 140th of the wavelength. The choice of meshing size has been validated.

Table 1. Geometry of the adaptive unit cell.

h_0	h_1	h_2	h_{s1}	h_{s2}	h_p	L	w_1
3 mm	3 mm	1 mm	2.6 mm	0.6 mm	0.2 mm	64 mm	5 mm

The effects of g on the wave velocity of sub-cell 1 and sub-cell 2 were investigated according to Equation (12) and are shown in Figure 3a. It can be observed from Figure 3a that the velocity of flexural waves rises as g increases. Therefore, the value of g was chosen to be 100 for sub-cell 1 and 0 for sub-cell 2, respectively. The phase shift and transmittance of adaptive unit cells when p varied from 0 to 1 were also examined with this prerequisite. The results obtained by the TMM were verified by comparison with those derived from the finite element method (FEM). To perform the FEM calculations, a location was selected for the phase and transmittance coefficient calculation in region IV, which was 240 mm away from the line connecting regions III and IV. It is worth noting that the absolute value of the phase can be altered if another point at a different location in the transmittance region is selected. However, the difference between the phase shift for the adaptive unit cell is always the same.

Figure 3b shows the transmission coefficient and phase shift versus the value of g when p = 0.5, and Figure 3c shows the phase shift and transmittance with respect to varying p as g was chosen as 100 for sub-cell 1 and 0 for sub-cell 2. In Figure 3b,c, the red solid line indicates the transmission coefficient resolved by the TMM, and the cyan dashed line indicates the numerical solution to the FEM. The black solid line and the dark yellow dashed line indicate the phase shifts obtained from the TMM and FEM calculations, respectively. As can be seen in Figure 3b, there is a very small error in the transmission coefficients calculated using the TMM and FEM; in fact, the maximum difference in values is within 0.05, while the phase gradient variation is achieved by adjusting the phase. We think that this produces a small effect on the tectonic metasurface. As can be seen in Figure 3b,c, the adaptive unit cell fails to cover a phase shift ranging from 0 to 2π when changing the control gain, but it can achieve this range with the change in p. According to the GSL, we used the adaptive unit cells to compose the column elastic metasurface by varying the parameters of the adaptive cells in order to effectively change the phase of each adaptive unit cell. We exploited this feature to construct a passive modulation metasurface by varying the adaptive unit cells of p and further varying g for active modulation based on it.

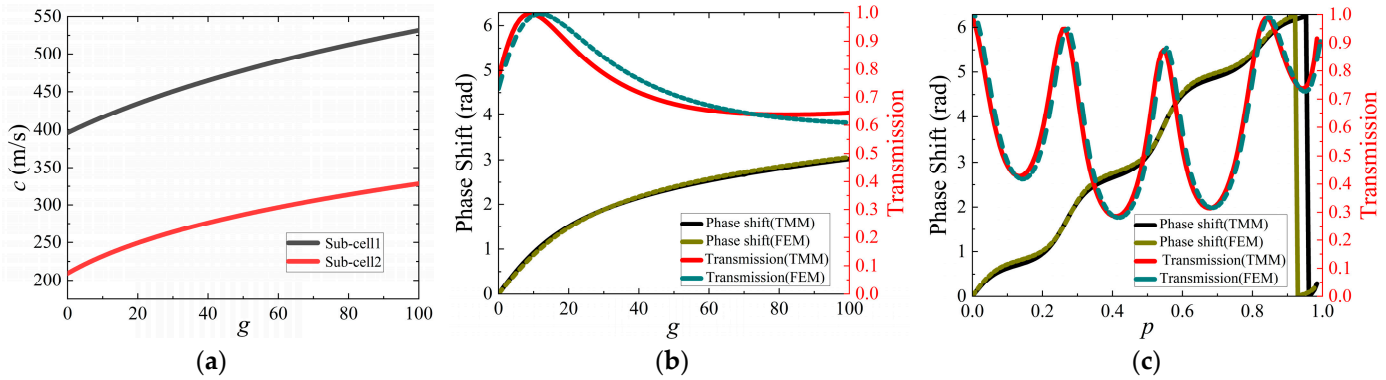

Figure 3. (**a**) The phase velocity curve varying with g for f = 6 kHz. (**b**) The transmission coefficient and phase shift as g increases while p = 0.5. (**c**) The transmission coefficient and phase shift with respect to varying p at 6 kHz when g is 100 in sub-cell 1 and 0 in sub-cell 2.

3.2. Results of Abnormal Transmittance

Based on the generalized Snell's law, different abnormal refraction strategies can be conducted by adjusting the adaptive unit cells of the metasurface. Additionally, it can be seen from Section 3.1 that the control gain (g) and p-values have an effect on the propagation of the flexural wave. Finite element simulation of flexural wave propagation was conducted using COMSOL Multiphysics software 6.0. Three-dimensional elements are adopted to discretize the incident field, the metasurface, and the transmitted field, whose size accounts for one 180th of the wavelength. The choice of meshing size has been validated. In order to achieve the abnormal refraction of flexural waves, 40 adaptive unit cells were utilized to form the metasurface, with a slit width w_2 of 1.98 mm between adaptive unit cells. Perfectly matched layers (PMLs) were arranged around the boundaries of the whole plate to eliminate the influence of reflected waves from boundaries (PML acts as a near-ideal wave absorber). A z-direction displacement $-1 \times \exp(-((y - 0)/\cos 0)^2/60^2)$ (mm) was applied at the boundary between the left PML and the incident plate to excite the flexural-wave Gaussian beam, and the wave in the plane surrounded by the black dashed line on the left side in Figure 4 represents the Gaussian beam. The wavelengths of flexural waves corresponding to f = 6 kHz and f = 7 kHz are 69.94 mm and 64.75 mm, respectively, within the 3 mm thick aluminum plate, satisfying the sub-wavelength requirement.

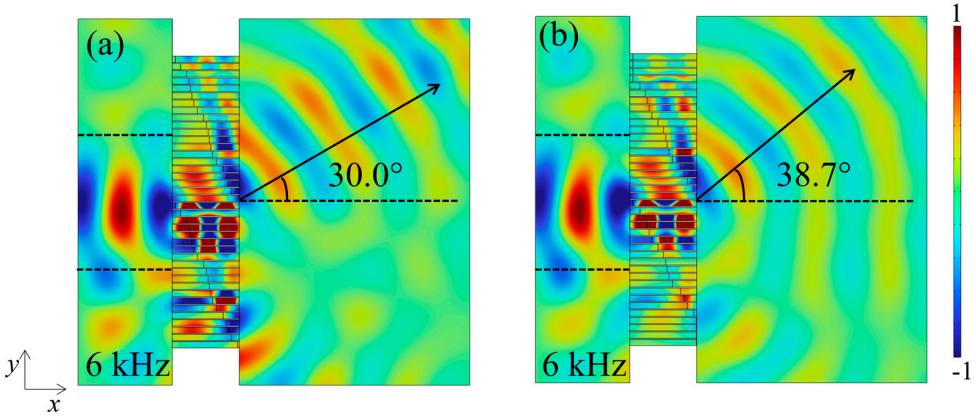

Figure 4. The out-of-plane displacement diagrams (z-direction) for flexural wave propagation with passive modulation by changing p at f = 6 kHz: the design refraction angles are (**a**) 30° and (**b**) 38.7°.

Firstly, the abnormal transmission of passively modulated metasurfaces was realized by changing p. Two different abnormal refraction angles, θ_t =30° and 38.7°, with operating frequency f = 6 kHz were designed as the targets. The g values for sub-cells 1 and 2 were assumed as 100 and 0, respectively, and the designed values of p were set to match the

requirement of phase shift ranging from 0 to 2π. The *p*-values of the R_ith adaptive cell units (R_i = 1 – 40) for different refraction angles in the case of f = 6 kHz are listed in Table A1 (θ_t = 30°, 38.7°). Full-wave simulations were performed, as shown in Figure 4a,b, from which it can be seen that the vertically incident Gaussian beam can be deflected on demand via the metasurface, realizing the abnormal transmission of the flexural waves. Obviously, the propagation of the transmitted wave matches very well with the theoretical design route.

Then, regarding the active modulation of flexural waves, the geometrical parameters of the unit cells were fixed, and abnormal transmission was achieved by varying the g from the negative proportional feedback control strategy applied in the sub-cells. The target angles for transmitted waves are assumed to be 20° and 38.7° when the incident frequency is 6 kHz, and at 7 kHz, these angles are assumed to be 20°, 30°, and 38.7°, respectively. Additionally, the used values of g for the active modulation are provided in Table A2, and the active tunability performance is shown in Figure 5. The simulated angles and target angles basically coincide with each other, which proves the effectiveness and reliability of the active metasurface based on the piezoelectrical effects and negative proportional feedback control technique. Meanwhile, the angles we designed are coincident at different operating frequencies, which suggests the reproducibility of the study. Moreover, it can be observed in Figures 4 and 5 that the main energy of the beam is concentrated in the designed deflection route, but there is still a small amount of energy appearing outside the designed angle, which belongs to the higher-order diffraction [51].

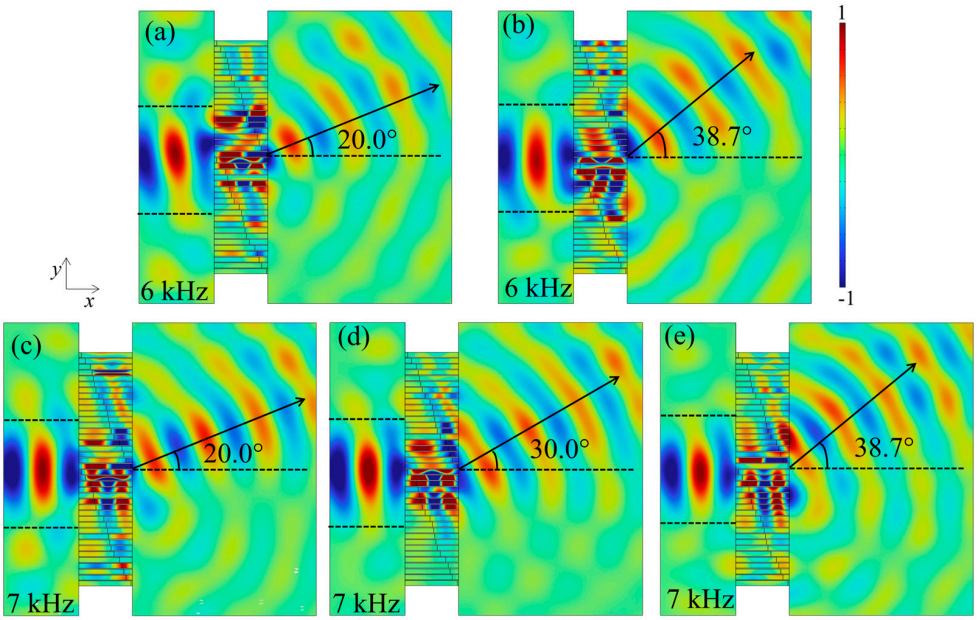

Figure 5. The out-of-plane displacement diagrams (*z*-direction) for flexural wave propagation with active modulation by changing g at f = 6 and 7 kHz: the design refractive angles are (**a**) 20°, (**b**) 38.7°, (**c**) 20°, (**d**) 30°, and (**e**) 38.7°, respectively.

3.3. Realization of Focus Functionality

In this subsection, the focusing functionality of flexural waves via the passively modulated and actively modulated metasurface is detailed separately. For a positively incident flexural wave, the phase distribution along the *x*-axis is calculated using Equation (17) within different operating frequencies and focusing point locations. The phase distribution is symmetrically distributed about the *y*-axis, and thus only 20 adaptive unit cells at one side of the *y*-axis need to be calculated.

In the FEM simulation, a unit displacement along the -*z* direction is applied to the left side of the metasurface for the excitation of the flexural wave. We designed passively modulated metasurfaces, which are expected to realize two focal points, (100 mm, 0) and (120 mm, 0), with different focal lengths at a functional frequency of 6 kHz by varying the *p*

and their design values, as shown in Table A1. Figure 6a,b show the numerically calculated out-of-plane displacement plots (*z*-direction) with the designed focal points (100 mm, 0) and (120 mm, 0) marked with black dashed crosses. It can be clearly seen that the flexural wave is incident vertically on the left side, and the transmitted wave on the right side produces a focusing phenomenon, with a clear focusing phenomenon at the position of the design focal point. To further demonstrate the flexural wave focusing effect obtained with our designed metasurface, the normalized displacement amplitude on the straight line $x = x_0$ where the focal point is located was calculated. Figure 7a,b show the normalized displacement amplitude on the line of $x = x_0$ where the design focus is located, in which the blue solid line is the displacement amplitude at $x = x_0$ and the horizontal blue dashed line denotes the displacement amplitude of the incident wave. From Figure 7, it can be seen that the vibration amplitude at the focal point of the design target is several times larger than the displacement amplitude of the incident wave, and the highest point of the amplitude is at $y = 0$ mm.

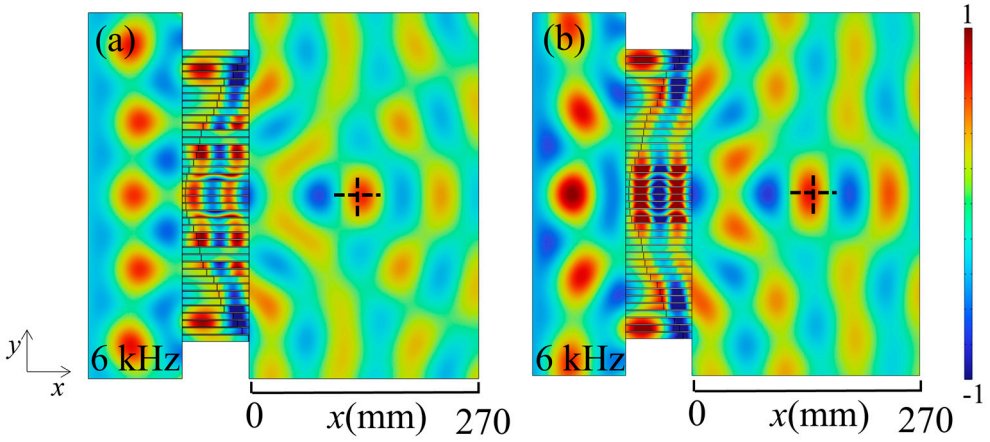

Figure 6. The out-of-plane displacement diagrams (*z*-direction) for flexural wave propagation with passive modulation by changing p at $f = 6$ kHz. The design focal positions were (**a**) (100 mm, 0) and (**b**) (120 mm, 0).

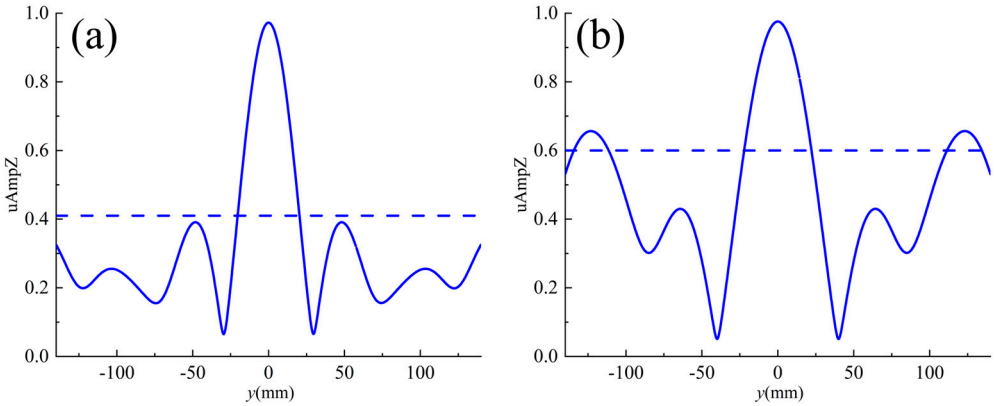

Figure 7. The normalized amplitude (*z*-component) of the displacement field along the straight line (**a**) $x_0 = 100$ mm and (**b**) $x_0 = 120$ mm when performing focusing (the vertical coordinate is the displacement amplitude).

Apart from passive adjustment, an actively metasurface was also designed to achieve the focusing of flexural waves. In this case, different focuses at different operating frequencies were required without changing the geometry of the metasurface. Table A3 presents the design values of g used in the sub-cells for achieving active wave focusing. From Figure 8a,b, it can be seen that the displacements of transmitted wave fields are concentrated in the positions (80 mm, 0) and (120 mm, 0), which is in accordance with the

design focal points at 6 kHz. Similarly, at another frequency of 7 kHz, three sets of focal points, (80 mm, 0), (100 mm, 0), and (120 mm, 0), were selected, and the verified performance is shown in Figure 8c–e. Figure 9a–e correspond sequentially to the normalized displacement amplitude on the line $x = x_{0,}$ where the focus is located in Figure 8a–e. As shown in Figure 9, the displacement amplitude at the focusing point far exceeds that of the surrounding region.

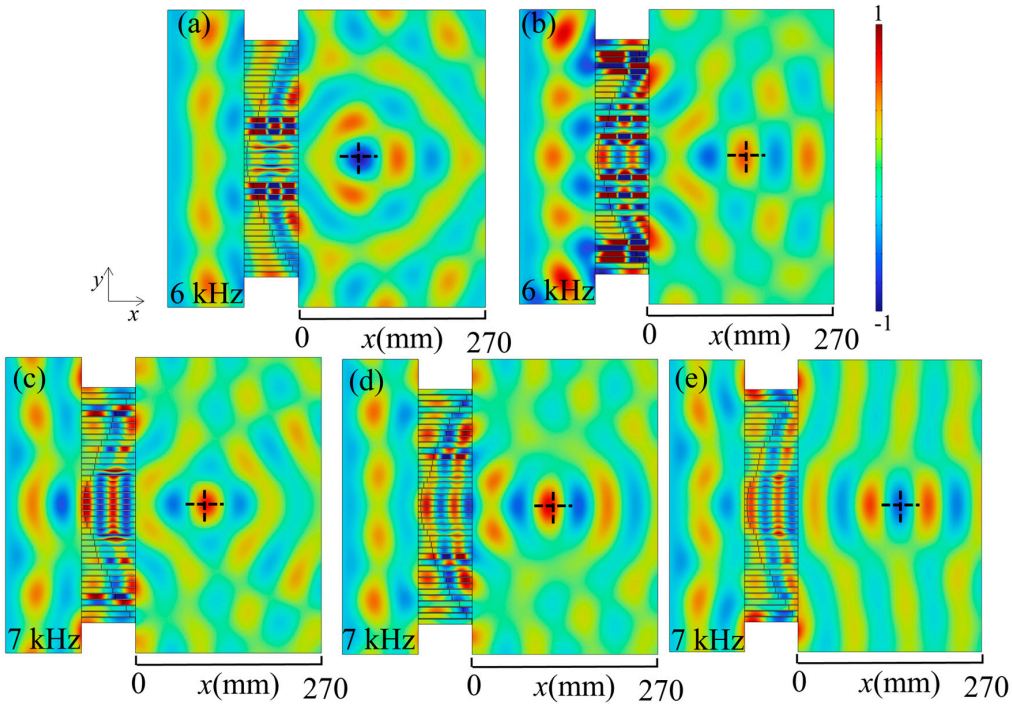

Figure 8. The out-of-plane displacement diagrams (*z*-direction) for flexural wave propagation with active modulation by changing g at f = 6 and 7 kHz. The design focal positions were (**a**) (80 mm, 0), (**b**) (120 mm, 0) (**c**) (80 mm, 0), (**d**) (100 mm, 0), and (**e**) (100 mm, 0).

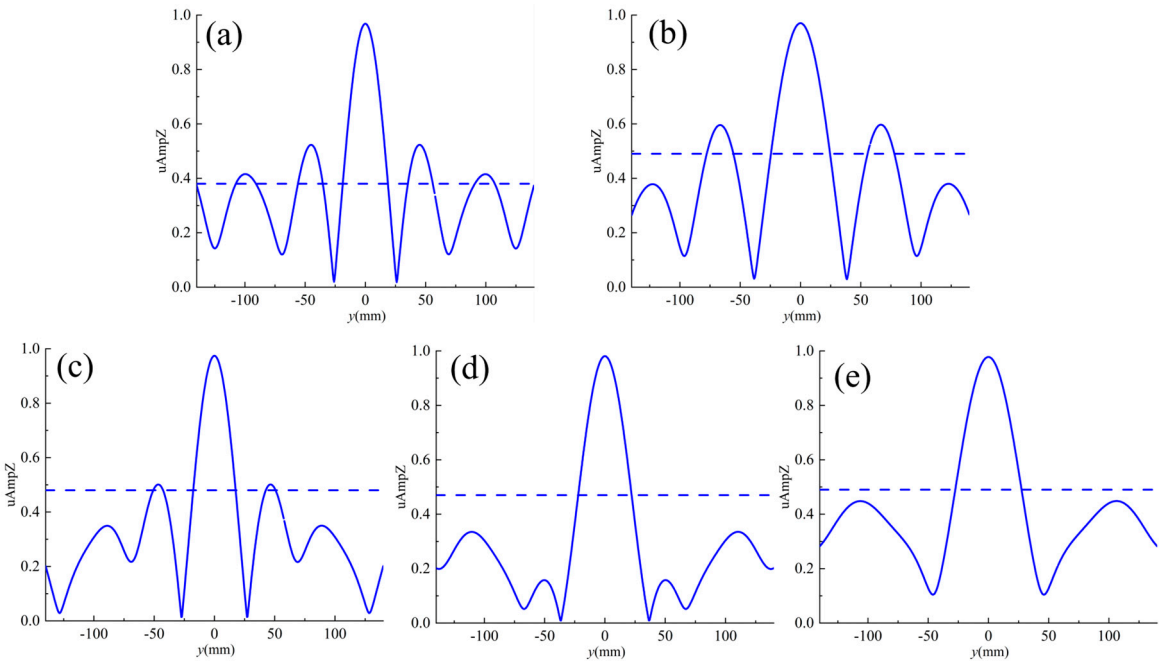

Figure 9. The normalized amplitude (*z*-component) for Figure 8. Values along the straight line are (**a**) x_0 = 100 mm, (**b**) x_0 = 120 mm, (**c**) x_0 = 80 mm, (**d**) x_0 = 100 mm, and (**e**) x_0 = 120 mm.

3.4. Transforming Guided Wave

In addition to the functions described above, the metasurface can also transform circular waves into plane waves. The transformation of the guided wave was investigated using a focused metasurface model (80 mm, 0) with a displacement in the -*z* direction applied at coordinates (*x*,*y*) = (−80 mm, 0) to excite the circular wave. Figure 10 shows the out-of-plane amplitude plot (*z*-direction) of a circular wave converted to a plane wave at operating frequencies of (a) f = 6 kHz and (b) 7 kHz. From Figure 10, it can be seen that the circular wave formed by the point source excitation as the incident applied on the left side can be successfully transformed into a plane wave when propagating through the transmitted field, completing the waveform transformation as designed. Numerical simulation results demonstrate that the metasurface not only achieves flexural wave focusing but also transforms circular waves into plane waves.

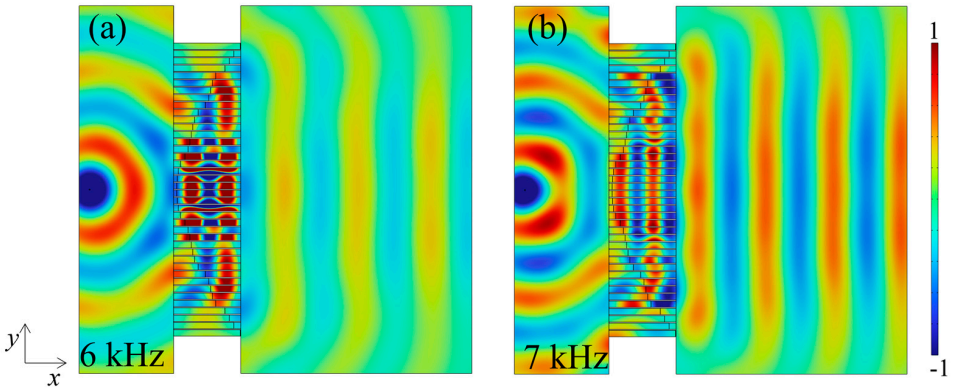

Figure 10. The out-of-plane displacement diagrams of the transforming guided wave at (**a**) f = 6 kHz and (**b**) 7 kHz.

4. Conclusions

In the present study, a tunable metasurface consisting of adaptive unit cells attached with piezoelectrical actuators and sensors was achieved by applying the negative proportional feedback control strategy. The flexural motion of the metasurface was derived based on the equivalent parameters of the adaptive unit cells. Employing the TMM, the analytical model was established to predict the transmittance and the phase shift of flexural waves propagating through the metasurface, and the validity was verified by comparing the results to those from FEM simulations. Based on the generalized Snell's law, a metasurface with 40 adaptive unit cells was designed. The passively modulated metasurface was constructed by changing the proportion of the adaptive unit cell occupied by sub-cells, and abnormal modulation flexural waves were achieved at 6 kHz. With the fixed geometrical parameters of the passively modulated metasurface, different phase gradients were generated by adjusting the negative proportional feedback system control gain. Full-wave simulations were performed in finite elements, and the metasurface achieved functions such as the abnormal transmission of multiple angles and the planar lensing of multiple positions at different operating frequencies. A comparison of the theoretical design and finite element simulations shows that this study is reproducible and reliable, which proves the feasibility of the design structure and method. The introduction of a negative proportional positive feedback control strategy provides an active method for adjusting the phase gradient to modulate flexural waves.

Author Contributions: Conceptualization, B.L. and J.L.; methodology, B.L. and J.L.; software, B.L. and J.L.; validation, B.L., J.L. and W.L.; formal analysis, B.L. and J.L.; investigation, J.L., W.L. and Q.M.; resources, B.L. and J.L.; data curation, B.L. and J.L.; writing—original draft preparation, B.L. and J.L.; writing—review and editing, B.L. and J.L.; visualization, B.L., J.L., W.L. and Q.M.; supervision, J.L.; project administration, J.L.; funding acquisition, J.L. All authors have read and agreed to the published version of the manuscript.

Funding: This research was funded by the National Natural Science Foundation of China, grant number 52365009, the Natural Science Foundation of Hainan Province, grant number 122MS004, and the Fundamental Research Funds for the Central Universities, grant number 3072022JC2601.

Institutional Review Board Statement: Not applicable.

Informed Consent Statement: Not applicable.

Data Availability Statement: The data presented in this study are available on request from the corresponding author due to privacy reasons.

Conflicts of Interest: The authors declare no conflicts of interest.

Appendix A

The following three tables show the p and g with values for the adaptive unit cells at different frequencies. Among them, Table A1 reflects the passively modulated metasurfaces to regulate the flexural wave by changing the geometrical structure, and Tables A2 and A3 reflect the use of control gain to regulate the flexural wave with fixed metasurface geometrical structure.

Table A1. The p of the R_ith adaptive unit cell for abnormal refraction and focusing in passive modulation.

R_i	The p of the Adaptive Unit Cell at 6 kHz			
	Abnormal Transmittance		Focusing	
	$\theta_t = 30^\circ$	$\theta_t = 38.7^\circ$	$x_0 = 100$ mm	$x_0 = 120$ mm
1	0.047	0.047	0.047	0.047
2	0.122	0.153	0.055	0.055
3	0.213	0.233	0.069	0.064
4	0.247	0.265	0.102	0.091
5	0.27	0.292	0.169	0.141
6	0.292	0.33	0.216	0.197
7	0.32	0.423	0.242	0.234
8	0.375	0.503	0.263	0.25
9	0.467	0.536	0.285	0.27
10	0.511	0.559	0.313	0.291
11	0.536	0.588	0.366	0.319
12	0.555	0.638	0.473	0.375
13	0.575	0.759	0.522	0.477
14	0.602	0.816	0.55	0.52
15	0.658	0.861	0.578	0.548
16	0.759	0.956	0.627	0.573
17	0.806	0.994	0.764	0.613
18	0.841	0.994	0.828	0.736
19	0.883	0.994	0.895	0.813
20	0.975	0.994	0.992	0.866
21	0.047	0.047		
22	0.122	0.047		
23	0.213	0.047		
24	0.247	0.047		
25	0.27	0.153		
26	0.292	0.233		
27	0.32	0.265		
28	0.375	0.292		
29	0.467	0.33		
30	0.511	0.423		
31	0.536	0.503		
32	0.555	0.536		
33	0.575	0.559		

Table A1. *Cont.*

R_i	The p of the Adaptive Unit Cell at 6 kHz			
	Abnormal Transmittance		Focusing	
	θ_t = 30°	θ_t = 38.7°	x_0 = 100 mm	x_0 = 120 mm
34	0.602	0.588		
35	0.658	0.638		
36	0.759	0.759		
37	0.806	0.816		
38	0.841	0.861		
39	0.883	0.956		
40	0.975	0.994		

Table A2. The g of the R_ith adaptive unit cell with abnormal refraction during active modulation.

R_i	The g of the Adaptive Unit Cell									
	6 kHz				7 kHz					
	θ_t = 20°		θ_t = 38.7°		θ_t = 20°		θ_t = 30°		θ_t = 38.7°	
	Sub-Cell1	Sub-Cell2	Sub-Cell1	Sub-Cell2	Sub-Cell1	Sub-Cell2	Sub-Cell1	Sub-Cell2	Sub-Cell1	Sub-Cell2
1	100	16.805	0	2.999	100	7.749	100	8.731	100	9.572
2	100	14.507	0	5.8	100	5.342	100	3.81	100	8.58
3	100	10.645	0	2.069	100	1.786	100	13.6	100	6.251
4	100	11.585	0	0.705	100	1.867	100	4.515	100	8.263
5	100	13.758	0	2.363	100	2.75	100	6.301	0.6	0
6	100	16.46	0	4.478	100	3.865	100	8.533	16.84	0
7	100	18.877	0	6.772	100	4.602	100	10.546	53.001	0
8	100	18.225	0	7.986	100	3.091	100	10.038	54.47	0
9	100	12.318	0	6.826	0	9.636	100	5.223	22.518	0
10	100	12.594	0	9.37	0	10.811	100	5.484	32.928	0
11	100	16.023	0	14.891	0	14.472	100	8.344	60.358	0
12	100	21.612	0	23.931	0	20.047	100	13.037	100	0.456
13	100	28.629	100	8.643	0	27.227	100	19.006	100	4.62
14	100	36.432	100	13.586	0	36.009	100	25.756	100	1.162
15	100	37.548	100	15.148	0	42.483	100	26.901	100	10.512
16	100	21.838	9.43	100	0	40.168	100	13.775	100	1.579
17	100	23.974	27.056	100	0	59.865	100	15.926	100	3.479
18	100	36.205	51.797	100	1.533	100	100	27.188	100	12.509
19	100	55.872	82.227	100	8.473	100	100	46.716	100	30.409
20	100	0	0	0	12.369	100	100	0	100	0
21	100	16.805	0	0	100	7.749	100	8.731	100	4.123
22	100	14.507	0	0.884	100	5.342	100	3.81	100	2.966
23	100	10.645	0	0.035	100	1.786	100	13.6	100	0.695
24	100	11.585	0	1.857	100	1.867	100	4.515	100	1.945
25	100	13.758	0	4.743	100	2.75	100	6.301	100	4.264
26	100	16.46	0	8.502	100	3.865	100	8.533	100	7.227
27	100	18.877	0	12.894	100	4.602	100	10.546	100	10.274
28	100	18.225	0	16.395	100	3.091	100	10.038	100	11.102
29	100	12.318	0	17.327	0	9.636	100	5.223	100	7.587
30	100	12.594	0	24.902	0	10.811	100	5.484	100	9.73
31	100	16.023	0	39.7	0	14.472	100	8.344	100	15.647
32	100	21.612	0	65.535	0	20.047	100	13.037	100	25.399
33	100	28.629	100	27.918	0	27.227	100	19.006	100	39.729
34	100	36.432	100	44.143	0	36.009	100	25.756	100	60.514
35	100	37.548	100	60.131	0	42.483	100	26.901	100	82.342
36	100	21.838	100	64.353	0	40.168	100	13.775	21.271	100
37	100	23.974	63.58	0	0	59.865	100	15.926	100	59.331
38	100	36.205	4.688	0	1.533	100	100	27.188	100	35.139
39	100	55.872	24.714	0	8.473	100	100	46.716	100	8.848
40	100	0	1.95	0	12.369	100	100	0	80.731	0

Table A3. The g of the R_ith adaptive unit cell with focusing during active modulation.

R_i	The g of the R_ith Adaptive Unit Cell									
	6 kHz				7 kHz					
	x_0 = 80 mm		x_0 = 120 mm		x_0 = 80 mm		x_0 = 100 mm		x_0 = 120 mm	
	Sub-Cell1	Sub-Cell2	Sub-Cell1	Sub-Cell2	Sub-Cell1	Sub-Cell2	Sub-Cell1	Sub-Cell2	Sub-Cell1	Sub-Cell2
1	0	1.435	0	3.533	0	1.73	0	1.93	0	3.534
2	0	1.497	0	3.527	0	1.816	0	1.958	0	3.529
3	0	1.674	0	3.508	0	1.962	0	2.077	0	3.509
4	0	1.485	0	2.984	0	1.746	0	1.736	0	2.985
5	0	0.192	0	1.254	0	0.525	0	0.167	0	1.25
6	0	0.06	0	0.559	0	0.311	0	0.065	0	0.56
7	0	1.038	0	0.97	0	1.127	0	0.662	0	0.971
8	0	2.752	0	3.002	0	5.623	0	2.328	0	1.946
9	0	1.599	0	3.283	0	4.663	0	4.612	0	3.285
10	0	4.53	0	4.819	0	3.176	0	7.419	0	4.82
11	0	6.835	0	5.322	0	4.997	0	9.412	0	5.324
12	0	5.714	0	3.5	0	3.515	0	7.637	0	2.414
13	0	10.698	2.94	0	0	7.347	0	12.01	2.947	0
14	0	21.957	18.275	0	0	16.2	0	22.068	18.285	0
15	0	42.822	39.794	0	0	32.079	0	39.881	39.808	0
16	0	83.017	51.791	0	0	60.175	0	71.127	51.808	0
17	10.033	100	16.464	0	1.457	100	83.942	0	16.474	0
18	34.214	100	19.949	0	21.692	100	89.628	0	19.959	0
19	66.646	100	22.789	0	48.817	100	93.326	0	22.8	0
20	98.763	100	17.278	0	76.565	100	74.579	0	17.288	0

References

1. Yi, K.; Collet, M.; Ichchou, M.; Li, L. Flexural waves focusing through shunted piezoelectric patches. *Smart Mater. Struct.* **2016**, *25*, 075007. [CrossRef]
2. Cao, L.; Yang, Z.; Xu, Y.; Fan, S.-W.; Zhu, Y.; Chen, Z.; Li, Y.; Assouar, B. Flexural wave absorption by lossy gradient elastic metasurface. *J. Mech. Phys. Solids* **2020**, *143*, 104052. [CrossRef]
3. Shen, Y.; Xu, Y.; Liu, F.; Yang, Z. Metasurface-guided flexural waves and their manipulations. *Int. J. Mech. Sci.* **2023**, *257*, 108538. [CrossRef]
4. Chen, A.-L.; Wang, Y.-S.; Wang, Y.-F.; Zhou, H.-T.; Yuan, S.-M. Design of Acoustic/Elastic Phase Gradient Metasurfaces: Principles, Functional Elements, Tunability, and Coding. *Appl. Mech. Rev.* **2022**, *74*, 020801. [CrossRef]
5. Wang, W.; Iglesias, J.; Jin, Y.; Djafari-Rouhani, B.; Khelif, A. Experimental realization of a pillared metasurface for flexural wave focusing. *APL Mater.* **2021**, *9*, 051125. [CrossRef]
6. Feng, L.; Liu, X.-P.; Lu, M.-H.; Chen, Y.-B.; Chen, Y.-F.; Mao, Y.-W.; Zi, J.; Zhu, Y.-Y.; Zhu, S.-N.; Ming, N.-B. Acoustic Backward-Wave Negative Refractions in the Second Band of a Sonic Crystal. *Phys. Rev. Lett.* **2006**, *96*, 014301. [CrossRef]
7. Lu, Y.; Srivastava, A. Level Repulsion and Band Sorting in Phononic Crystals. *J. Mech. Phys. Solids* **2017**, *111*, 100–112. [CrossRef]
8. Liu, Z.; Zhang, X.; Mao, Y.; Zhu, Y.Y.; Yang, Z.; Chan, C.T.; Sheng, P. Locally Resonant Sonic Materials. *Science* **2000**, *289*, 1734–1736. [CrossRef] [PubMed]
9. Oh, J.H.; Kwon, Y.E.; Lee, H.J.; Kim, Y.Y. Elastic metamaterials for independent realization of negativity in density and stiffness. *Sci. Rep.* **2016**, *6*, 23630. [CrossRef] [PubMed]
10. Reynolds, M.; Daley, S. An active viscoelastic metamaterial for isolation applications. *Smart Mater. Struct.* **2014**, *23*, 045030. [CrossRef]
11. Sun, S.; He, Q.; Xiao, S.; Xu, Q.; Li, X.; Zhou, L. Gradient-index meta-surfaces as a bridge linking propagating waves and surface waves. *Nat. Mater.* **2012**, *11*, 426–431. [CrossRef]
12. Yu, N.; Capasso, F. Flat optics with designer metasurfaces. *Nat. Mater.* **2014**, *13*, 139–150. [CrossRef]
13. Zhang, J.; Kosugi, Y.; Otomo, A.; Nakano, Y.; Tanemura, T. Active metasurface modulator with electro-optic polymer using bimodal plasmonic resonance. *Opt. Express* **2017**, *25*, 30304–30311. [CrossRef]
14. Qi, S.; Li, Y.; Assouar, B. Acoustic Focusing and Energy Confinement Based on Multilateral Metasurfaces. *Phys. Rev. Appl.* **2017**, *7*, 054006. [CrossRef]
15. Xie, B.; Tang, K.; Cheng, H.; Liu, Z.; Chen, S.; Tian, J. Coding Acoustic Metasurfaces. *Adv. Mater.* **2017**, *29*, 1603507. [CrossRef] [PubMed]
16. Liang, Z.; Li, J. Extreme Acoustic Metamaterial by Coiling Up Space. *Phys. Rev. Lett.* **2012**, *108*, 114301. [CrossRef] [PubMed]

17. Fan, S.-W.; Zhao, S.-D.; Cao, L.; Zhu, Y.; Chen, A.-L.; Wang, Y.-F.; Donda, K.; Wang, Y.-S.; Assouar, B. Reconfigurable curved metasurface for acoustic cloaking and illusion. *Phys. Rev. B* **2020**, *101*, 024104. [CrossRef]
18. Li, Y.; Liang, B.; Gu, Z.-M.; Zou, X.-Y.; Cheng, J.-C. Reflected wavefront manipulation based on ultrathin planar acoustic metasurfaces. *Sci. Rep.* **2013**, *3*, 2546. [CrossRef] [PubMed]
19. Schwan, L.; Umnova, O.; Boutin, C. Sound absorption and reflection from a resonant metasurface: Homogenisation model with experimental validation. *Wave Motion* **2017**, *72*, 154–172. [CrossRef]
20. Shen, Y.; Xu, Y.; Liu, F.; Wang, F.; Yang, Z. 3D-printed meta-slab for focusing flexural waves in broadband. *Extrem. Mech. Lett.* **2021**, *48*, 101410. [CrossRef]
21. Zhu, H.; Semperlotti, F. Anomalous Refraction of Acoustic Guided Waves in Solids with Geometrically Tapered Metasurfaces. *Phys. Rev. Lett.* **2016**, *117*, 034302. [CrossRef]
22. Zeng, L.; Zhang, J.; Liu, Y.; Zhao, Y.; Hu, N. Asymmetric transmission of elastic shear vertical waves in solids. *Ultrasonics* **2019**, *96*, 34–39. [CrossRef] [PubMed]
23. Hu, Y.; Li, M.; Liu, H.; Li, B. Broadband manipulation of flexural waves based on phase-modulated elastic metasurfaces. *Eng. Struct.* **2023**, *275*, 115209. [CrossRef]
24. Kim, M.S.; Lee, W.R.; Kim, Y.Y.; Oh, J.H. Transmodal elastic metasurface for broad angle total mode conversion. *Appl. Phys. Lett.* **2018**, *112*, 241905. [CrossRef]
25. Tian, Z.; Yu, L. Elastic Phased Diffraction Gratings for Manipulation of Ultrasonic Guided Waves in Solids. *Phys. Rev. Appl.* **2019**, *11*, 024052. [CrossRef]
26. Lee, H.; Lee, J.K.; Seung, H.M.; Kim, Y.Y. Mass-stiffness substructuring of an elastic metasurface for full transmission beam steering. *J. Mech. Phys. Solids* **2018**, *112*, 577–593. [CrossRef]
27. Xu, Y.; Zhou, X.; Wang, W.; Wang, L.; Peng, F.; Li, B. On natural frequencies of non-uniform beams modulated by finite periodic cells. *Phys. Lett. A* **2016**, *380*, 3278–3283. [CrossRef]
28. Cao, L.; Yang, Z.; Xu, Y. Steering elastic SH waves in an anomalous way by metasurface. *J. Sound Vib.* **2018**, *418*, 1–14. [CrossRef]
29. Xu, Y.; Cao, L.; Peng, P.; Zhou, X.; Assouar, B.; Yang, Z. Beam splitting of flexural waves with a coding meta-slab. *Appl. Phys. Express* **2019**, *12*, 097002. [CrossRef]
30. Zhu, H.; Walsh, T.F.; Semperlotti, F. Total-internal-reflection elastic metasurfaces: Design and application to structural vibration isolation. *Appl. Phys. Lett.* **2018**, *113*, 221903. [CrossRef]
31. Liu, Y.; Liang, Z.; Liu, F.; Diba, O.; Lamb, A.; Li, J. Source Illusion Devices for Flexural Lamb Waves Using Elastic Metasurfaces. *Phys. Rev. Lett.* **2017**, *119*, 034301. [CrossRef]
32. Cao, L.; Yang, Z.; Xu, Y.; Fan, S.-W.; Zhu, Y.; Chen, Z.; Vincent, B.; Assouar, B. Disordered Elastic Metasurfaces. *Phys. Rev. Appl.* **2020**, *13*, 014054. [CrossRef]
33. Su, X.; Lu, Z.; Norris, A.N. Elastic metasurfaces for splitting SV- and P-waves in elastic solids. *J. Appl. Phys.* **2018**, *123*, 091701. [CrossRef]
34. Lin, Z.; Xu, W.; Xuan, C.; Qi, W.; Wang, W. Modular elastic metasurfaces with mass oscillators for transmitted flexural wave manipulation. *J. Phys. D Appl. Phys.* **2021**, *54*, 255303. [CrossRef]
35. Xu, W.; Zhang, M.; Lin, Z.; Liu, C.; Qi, W.; Wang, W. Anomalous refraction manipulation of Lamb waves using single-groove metasurfaces. *Phys. Scr.* **2019**, *94*, 105807. [CrossRef]
36. Zhou, W.; Wang, S.; Wu, Q.; Xu, X.; Huang, X.; Huang, G.; Liu, Y.; Fan, Z. An inverse design paradigm of multi-functional elastic metasurface via data-driven machine learning. *Mater. Des.* **2023**, *226*, 111560. [CrossRef]
37. Yuan, S.-M.; Chen, A.-L.; Du, X.-Y.; Zhang, H.-W.; Assouar, B.; Wang, Y.-S. Reconfigurable flexural waves manipulation by broadband elastic metasurface. *Mech. Syst. Signal Process.* **2022**, *179*, 109371. [CrossRef]
38. Li, S.; Xu, J.; Tang, J. Tunable modulation of refracted lamb wave front facilitated by adaptive elastic metasurfaces. *Appl. Phys. Lett.* **2018**, *112*, 021903. [CrossRef]
39. Shao, S.; Xia, R.; Li, Z. Tunable piezoelectric metasurface for manipulating multi-mode guided waves in plate. *Eng. Struct.* **2022**, *270*, 114917. [CrossRef]
40. Ren, T.; Liu, C.; Li, F.; Zhang, C. Active tuning of the vibration band gap characteristics of periodic laminated composite metamaterial beams. *J. Intell. Mater. Syst. Struct.* **2020**, *31*, 843–859. [CrossRef]
41. Liu, F.; Shi, P.; Chen, Z.; Shen, Y.; Xu, Y.; Yang, Z. Tunable reflection and broadband absorption of flexural waves by adaptive elastic metasurface with piezoelectric shunting circuits. *Smart Mater. Struct.* **2023**, *32*, 055018. [CrossRef]
42. Yaw, Z.; Zhou, W.; Chen, Z.; Lim, C. Stiffness tuning of a functional-switchable active coding elastic metasurface. *Int. J. Mech. Sci.* **2021**, *207*, 106654. [CrossRef]
43. Li, B.; Hu, Y.; Chen, J.; Su, G.; Liu, Y.; Zhao, M.; Li, Z. Efficient Asymmetric Transmission of Elastic Waves in Thin Plates with Lossless Metasurfaces. *Phys. Rev. Appl.* **2020**, *14*, 054029. [CrossRef]
44. Xu, Y.; Cao, L.; Yang, Z. Deflecting incident flexural waves by nonresonant single-phase meta-slab with subunits of graded thicknesses. *J. Sound Vib.* **2019**, *454*, 51–62. [CrossRef]
45. Qiu, H.; Chen, M.; Huan, Q.; Li, F. Steering and focusing of fundamental shear horizontal guided waves in plates by using multiple-strip metasurfaces. *Europhys. Lett.* **2019**, *127*, 46004. [CrossRef]
46. Lin, Z.; Tol, S. Electroelastic metasurface with resonant piezoelectric shunts for tunable wavefront control. *J. Phys. D Appl. Phys.* **2023**, *56*, 164001. [CrossRef]

47. Chen, Y.; Li, X.; Nassar, H.; Hu, G.-K.; Huang, G. A programmable metasurface for real time control of broadband elastic rays. *Smart Mater. Struct.* **2018**, *27*, 115011. [CrossRef]
48. Wang, G.; Chen, S.; Wen, J. Low-frequency locally resonant band gaps induced by arrays of resonant shunts with Antoniou's circuit: Experimental investigation on beams. *Smart Mater. Struct.* **2010**, *20*, 015026. [CrossRef]
49. Zhang, H.; Wen, J.-H.; Chen, S.-B.; Wang, G.; Wen, X.-S. Flexural wave band-gaps in phononic metamaterial beam with hybrid shunting circuits. *Chin. Phys. B* **2015**, *24*, 036201. [CrossRef]
50. Li, F.; Zhang, C.; Liu, C. Active tuning of vibration and wave propagation in elastic beams with periodically placed piezoelectric actuator/sensor pairs. *J. Sound Vib.* **2017**, *393*, 14–29. [CrossRef]
51. Xu, Y.; Yang, Z.; Cao, L. Deflecting Rayleigh surface acoustic waves by a meta-ridge with a gradient phase shift. *J. Phys. D Appl. Phys.* **2018**, *51*, 175106. [CrossRef]